A STUDY OF FAST MULTIPOLE METHOD ON THE ANALYSIS OF 2D BARRIER

C.-H. Wu [*] **C.-N. Wang** [**]

Department of Engineering Science and Ocean Engineering
National Taiwan University
Taipei, Taiwan 10617, R.O.C.

T.-D. Wu [***]

Department of Industrial Engineering and Management
Tungnan University
Taipei, Taiwan 22202, R.O.C.

ABSTRACT

The purpose of this paper is to investigate, by the Fast Multipole Method (FMM), the sound field for a rigid barrier located on flat ground. At first the governed Helmholtz equation is transformed to a boundary integral equation, and then it is expressed as the summation of the integration of individual element. FMM is adopted to accelerate the speed of calculation. By an addition theorem, the kernels in the integral can be expanded to degenerate kernels, which separate the source point and field point. Compared with conventional BEM, FMM can reduce CPU time from $O(N^2)$ to $O(N \log^{\gamma}(N))$ where N is the number of unknowns and γ is a non-negative small number. Since the expansion is an infinite series, this number of terms is needed to satisfy the accuracy of computation and will be discussed. Finally, the effects of the rectangular, *T*-shaped, and *Y*-shaped barriers on noise reduction are also investigated.

Keywords : FMM, Barrier, Exterior acoustic problem and insertion loss.

1. INTRODUCTION

Barriers are widely used to reduce outdoor propagation noise. Thus, many researches about barriers have been done. Hothersall *et al.* [1] discussed many different shaped barriers — cross-sectional, semi-circular, broad wedged and spectral using the boundary element method (BEM). Kawai and Terai [2] applied integral equation derived from Helmholtz-Kirchhoff's formula and from its normal derivative to solve thin rigid or absorbent barriers. The BEM numerical modeling was adopted to solve the insertion loss of rectangular, *T*-shaped, and cylindrical edged noise barriers with rigid, absorbing and soft surfaces by Fujiwara *et al.* [3] and they compared well with the measured data. Lam [4] estimated the insertion loss of the finite length barriers by Maekawa's chart. Muradali and Fyfe [5] analyzed 2D, 3D finite, and 3D infinite barriers and compared them with those results from by Lam's method via Maekawa's curve and Lam's method via Kurze and Anderson's equations.

In general, for the analysis of a barrier, BEM [6] is more suitable than the domain methods such as the finite element method (FEM) [7-9] and the finite difference method (FDM), which have to mesh the infinite domain. However, the coefficient matrices established by BEM are full and often non-symmetric. The CPU time is about the order of N^2. When the scale is very large, it costs a lot of CPU time and memory to build the matrices. Sometimes it is impractical. FMM is a technique which is based on separating the field points and source points to approach the solution of problems. For FMM, the CPU time is reduced to an order of $N\log^{\gamma}N$. Obviously, this method is more suitable for adopting to solve present problems.

Rokhlin [10] researched the potential problem and inaugurated the history of FMM in 1985. This method was further developed by Greengard [11] for the pairwise force calculation with Coulombic or gravitational potential. Therefore, FMM was applied to all sorts of studies. Chen *et al.* [12] solved the 2D exterior acoustic problem and successfully expanded the four kernels in the dual formulation into degenerate kernels that separated the field and source points by the addition theory. Chen *et al.* [13] adopted the concept of FMM to solve a rigid thin barrier at the normal and oblique incident wave, and the results are compared well with those of BEM and analytical solutions. Fujiwara [14,15] adopted the FMM to solve the three-

[*] Ph.D. candidate [**] Professor [***] Assistant Professor

dimensional topography, basin and seismic scattering problems. Nishimura [16] discussed the research of FMM for Laplace, Helmholtz, and the heat equation in detail.

It was found that there were few attempts via the FMM in the discussion of acoustic problems in the semi-infinite region. Therefore, in this study we will employ the FMM to analyze the noise distribution around a 2D barrier. Further, the influence of different barrier shapes and breadths will also be investigated.

2. BASIC FORMULATION

We consider that a sound wave propagates over a rigid noise barrier on flat ground, as shown in Fig. 1. When a sound wave is incident upon the barrier, the sound pressure on the boundary of the barrier can be expressed as [3,17]

$$C(\bar{\xi})P(\bar{\xi}) = \int_{\Gamma} G(\bar{\xi},\ \bar{s})\frac{\partial P(\bar{s})}{\partial n(\bar{s})}d\Gamma(\bar{s}) - \int_{\Gamma}\frac{\partial G(\bar{\xi},\ \bar{s})}{\partial n(\bar{s})}P(\bar{s})\ d\Gamma(\bar{s}) + P_I(\bar{\xi}),\ \bar{\xi}\in\Gamma\ , \quad (1)$$

where

$$P(\bar{\xi}) = p_i(\bar{\xi}) + p_\infty(\bar{\xi}) + p_r(\bar{\xi}) + p_d(\bar{\xi})\ , \quad (2)$$

$$P_I(\bar{\xi}) = p_i(\bar{\xi}) + p_\infty(\bar{\xi})\ . \quad (3)$$

P_i is the incident sound wave, P_r is the radiated wave from the barrier, P_d is the diffracted wave from the barrier, P_∞ is the reflective wave from the infinite plane or called an image incident wave, $\bar{\xi}$ is the field point, $\bar{s}$ is the source point, $\partial/\partial n(\bar{s})$ indicates a normal derivative at source point and Γ denotes the boundary, not including Γ_G as show in Fig. 1. The coefficient $C(\bar{\xi})$ depends on the position of $\bar{\xi}$. If $\bar{\xi}$ is a point on Γ which is not a corner, the coefficient $C(\bar{\xi}) = 1/2$; if $\bar{\xi}$ is a corner point, we can obtain $C(\bar{\xi}) = \Theta/2\pi$, where Θ is the angle in the medium subtended by the two tangents to the boundary at $\bar{\xi}$. When the ground is rigid and flat, the half-space fundamental solution of Helmholtz equation is easy to obtain by the method of images and that is expressed as [3]

$$G(\bar{\xi},\ \bar{s}) = \frac{1}{4i}\left[H_0^{(2)}\left(k\,|\,\bar{\xi}-\bar{s}\,|\right) + H_0^{(2)}\left(k\,|\,\bar{\xi}-\bar{s}'\,|\right)\right]\ , \quad (4)$$

where $H_0^{(2)}(\zeta)$ denotes the Hankel function of the second kind zeroth order, $\bar{s}'$ is the image of the source point, k is the wave number, and i is the square root of -1.

To solve the problem, the boundary is divided into N elements and assumes that the physical quantities are constant on each element Γ_β. Then Eq. (1) is expressed as

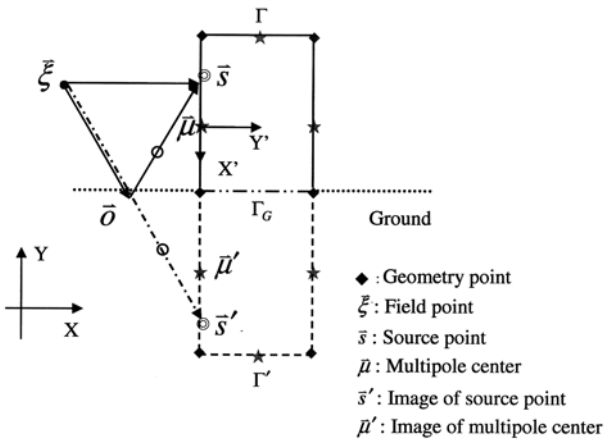

Fig. 1 The global coordinate (X, Y) and local coordinate (X', Y')

$$\frac{1}{2}P(\bar{\xi}) = \sum_{\beta=1}^{N}\frac{\partial P(\bar{s})}{\partial n(\bar{s})}\int_{\Gamma_\beta} G(\bar{\xi},\ \bar{s})\ d\Gamma_\beta(\bar{s}) - \sum_{\beta=1}^{N}P(\bar{s})\int_{\Gamma_\beta}\frac{\partial G(\bar{\xi},\ \bar{s})}{\partial n(\bar{s})}\ d\Gamma_\beta(\bar{s}) + P_I(\bar{\xi}),\ \bar{\xi}\in\Gamma\ . \quad (5)$$

Applying Eq. (5) on each node and conducting the integration on each element, the system equations expressed in matrix form is

$$[A]\{P(\bar{s})\} = [B]\left\{\frac{\partial P(\bar{s})}{\partial n(\bar{s})}\right\} + P_I(\bar{\xi}) \quad (6)$$

where $P(\bar{s})$ 、$\dfrac{\partial P(\bar{s})}{\partial n(\bar{s})}$ are the column vectors of pressure and pressure gradient, respectively. $A_{\alpha\beta} = \dfrac{1}{2}\delta_{\alpha\beta} + \int_{\Gamma_\beta}\dfrac{\partial G(\bar{\xi},\ \bar{s})}{\partial n(\bar{s})}\ d\Gamma_\beta$, $B_{\alpha\beta} = \int_{\Gamma_\beta} G(\bar{\xi},\ \bar{s})\ d\Gamma_\beta$ denote the matrix coefficients, the subscripts α and β correspond to the labels of the collocation element and integration element, respectively. When $\alpha = \beta$, the constant $\delta_{\alpha\beta} = 1$; otherwise it is zero.

To analyze an exterior problem via the boundary element method, it will cause the non-uniqueness solution to be at a specific frequency. Chen *et al*. [18] applied the complex-valued BEM to explain the reason why fictitious frequency occurs in exterior acoustics. The CHIEF method [19] or the Burton and Miller method [20] is the public manner to solve the non-uniqueness problem. For simplicity, the CHIEF method is adopted to solve the non-uniqueness problem in this study. For points located inside the barrier, the CHIEF equation is expressed as:

$$0 = \int_{\Gamma} G(\bar{\xi},\ \bar{s})\frac{\partial P(\bar{s})}{\partial n(\bar{s})}\ d\Gamma(\bar{s}) - \int_{\Gamma}\frac{\partial G(\bar{\xi},\ \bar{s})}{\partial n(\bar{s})}P(\bar{s})\ d\Gamma(\bar{s}) + P_I(\bar{\xi})\ . \quad (7)$$

With Eqs (6) and (7), the pressure distribution on the barrier can be solved, and consequently the field sound pressure can also be evaluated. Then the insertion loss is adopted to illustrate the efficiency of the barrier and is expressed as [3]

$$IL = 20\log_{10}\left|\frac{p_g}{p_b}\right| \text{ dB}, \tag{8}$$

where p_g is the sound pressure at the receiver without a barrier and p_b is the sound pressure at the receiver for the same ground conditions with the barrier.

3. THE FAST MULTIPOLE METHOD

First of all, the kernel functions $G(\bar{\xi}, \bar{s})$ and $G_n = \dfrac{\partial G(\bar{\xi}, \bar{s})}{\partial n(\bar{s})}$ can be obtained from the boundary integral formulation. It clearly shows the relationship between field and source points. Therefore, the kernel functions can be separated the field points and source points into two terms by the addition theorem [12,21] as shown in the following equations:

$$G(\bar{\xi}, \bar{s}) = \begin{cases} G^R = -\dfrac{i}{4}\displaystyle\sum_{m=-\infty}^{\infty}\Big[H_m^{(2)}\left(k\,|\,\bar{\xi}-\bar{\mu}\,|\right)J_m\left(k\,|\,\bar{s}-\bar{\mu}\,|\right)\cos(m\theta)+ \\ \qquad H_m^{(2)}\left(k\,|\,\bar{\xi}-\bar{\mu}'\,|\right)J_m\left(k\,|\,\bar{s}'-\bar{\mu}'\,|\right)\cos(m\theta')\Big], & |\bar{\xi}-\bar{\mu}| > |\bar{s}-\bar{\mu}| \\ G^S = -\dfrac{i}{4}\displaystyle\sum_{m=-\infty}^{\infty}\Big[J_m\left(k\,|\,\bar{\xi}-\bar{\mu}\,|\right)H_m^{(2)}\left(k\,|\,\bar{s}-\bar{\mu}\,|\right)\cos(m\theta)+ \\ \qquad J_m\left(k\,|\,\bar{\xi}-\bar{\mu}'\,|\right)H_m^{(2)}\left(k\,|\,\bar{s}'-\bar{\mu}'\,|\right)\cos(m\theta')\Big], & |\bar{\xi}-\bar{\mu}| < |\bar{s}-\bar{\mu}| \end{cases} \tag{9}$$

where $\bar{\mu}$ is the center of multipole, $J_m(\zeta)$ denotes the Bessel function of the first kind and ζ is an argument.

Taking the normal derivative with $G(\bar{\xi}, \bar{s})$ at source point, the function $G_n(\bar{\xi}, \bar{s})$ can be derived and displayed in the following equations:

$$G_n(\bar{\xi}, \bar{s}) = \begin{cases} G_n^R = -\dfrac{i}{4}\displaystyle\sum_{m=-\infty}^{\infty}\Big\{H_m^{(2)}\left(k\,|\,\bar{\xi}-\bar{\mu}\,|\right)\frac{\partial}{\partial n(\bar{s})}\Big[J_m\left(k\,|\,\bar{s}-\bar{\mu}\,|\right)\cos(m\theta)\Big]+ \\ \qquad H_m^{(2)}\left(k\,|\,\bar{\xi}-\bar{\mu}'\,|\right)\frac{\partial}{\partial n(\bar{s})}\Big[J_m\left(k\,|\,\bar{s}'-\bar{\mu}'\,|\right)\cos(m\theta')\Big]\Big\}, & |\bar{\xi}-\bar{\mu}| > |\bar{s}-\bar{\mu}| \\ G_n^S = -\dfrac{i}{4}\displaystyle\sum_{m=-\infty}^{\infty}\Big\{J_m\left(k\,|\,\bar{\xi}-\bar{\mu}\,|\right)\frac{\partial}{\partial n(\bar{s})}\Big[H_m^{(2)}\left(k\,|\,\bar{s}-\bar{\mu}\,|\right)\cos(m\theta)\Big]+ \\ \qquad J_m\left(k\,|\,\bar{\xi}-\bar{\mu}'\,|\right)\frac{\partial}{\partial n(\bar{s})}\Big[H_m^{(2)}\left(k\,|\,\bar{s}'-\bar{\mu}'\,|\right)\cos(m\theta')\Big]\Big\}, & |\bar{\xi}-\bar{\mu}| < |\bar{s}-\bar{\mu}| \end{cases} \tag{10}$$

The partial derivatives of Hankel, Bessel, and the cosine functions are displayed as follows:

$$\frac{\partial}{\partial n(\bar{s})}\left(J_m\left(k\,|\,\bar{s}-\bar{\mu}\,|\right)\right) = \frac{k}{2}\Big[J_{m-1}\left(k\,|\,\bar{s}-\bar{\mu}\,|\right)-J_{m+1}\left(k\,|\,\bar{s}-\bar{\mu}\,|\right)\Big]\frac{(s_x-\mu_x)\,n_x(\bar{s})+(s_y-\mu_y)\,n_y(\bar{s})}{|\,\bar{s}-\bar{\mu}\,|}, \tag{11}$$

$$\frac{\partial}{\partial n(\bar{s})}\left(J_m\left(k\,|\,\bar{s}'-\bar{\mu}'\,|\right)\right) = \frac{k}{2}\left(J_{m-1}\left(k\,|\,\bar{s}'-\bar{\mu}'\,|\right)-J_{m+1}\left(k\,|\,\bar{s}'-\bar{\mu}'\,|\right)\right)\frac{(s_x-p_x)\,n_x(\bar{s})-(-s_y+p_y)\,n_y(\bar{s})}{|\,\bar{s}'-\bar{\mu}'\,|}, \tag{12}$$

$$\frac{\partial}{\partial n(\bar{s})}\left(H_m^{(2)}\left(k\,|\,\bar{s}-\bar{\mu}\,|\right)\right) = \frac{k}{2}\Big[H_{m-1}^{(2)}\left(k\,|\,\bar{s}-\bar{\mu}\,|\right)-H_{m+1}^{(2)}\left(k\,|\,\bar{s}-\bar{\mu}\,|\right)\Big]\frac{(s_x-\mu_x)\,n_x(\bar{s})+(s_y-\mu_y)\,n_y(\bar{s})}{|\,\bar{s}-\bar{\mu}\,|}, \tag{13}$$

$$\frac{\partial}{\partial n(\bar{s})}\left(H_m^{(2)}\left(k\,|\,\bar{s}'-\bar{\mu}'\,|\right)\right) = \frac{k}{2}\left[H_{m-1}^{(2)}\left(k\,|\,\bar{s}'-\bar{\mu}'\,|\right)-H_{m+1}^{(2)}\left(k\,|\,\bar{s}'-\bar{\mu}'\,|\right)\right]\frac{(s_x-\mu_x)\,n_x(\bar{s})-(-s_y-\mu_y)\,n_y(\bar{s})}{|\,\bar{s}'-\bar{\mu}'\,|}\ , \tag{14}$$

$$\frac{\partial}{\partial n(\bar{s})}\cos(m\theta) = -m\sin(m\theta)\frac{-1}{\sin\theta}\left[a_x^1\,n_x(\bar{s})+a_y^1\,n_y(\bar{s})\right]\ , \tag{15}$$

$$a_x^1 = \frac{(s_y-\mu_y)^2(\xi_x-\mu_x)-(s_x-\mu_x)(s_y-\mu_y)(\xi_y-\mu_y)}{|\,\bar{s}-\bar{\mu}\,|^3|\,\bar{\xi}-\bar{\mu}\,|}\ , \tag{16}$$

$$a_y^1 = \frac{(s_x-\mu_x)^2(\xi_y-\mu_y)-(s_x-\mu_x)(s_y-\mu_y)(\xi_x-\mu_x)}{|\,\bar{s}-\bar{\mu}\,|^3|\,\bar{\xi}-\bar{\mu}\,|}\ , \tag{17}$$

$$\frac{\partial}{\partial n(\bar{s})}\cos(m\theta') = -m\sin(m\theta')\frac{-1}{\sin\theta'}\left[a_x^2\,n_x(\bar{s})+a_y^2\,n_y(\bar{s})\right]\ , \tag{18}$$

$$a_x^2 = \frac{(-s_y+\mu_y)^2(\xi_x-\mu_x)-(s_x-\mu_x)(-s_y+\mu_y)(\xi_y+\mu_y)}{|\,\bar{s}-\bar{\mu}\,|^3|\,\bar{\xi}-\bar{\mu}\,|}\ , \tag{19}$$

$$a_y^2 = -\frac{(s_x-\mu_x)^2(\xi_y+\mu_y)+(s_x-\mu_x)(-s_y+\mu_y)(\xi_x-\mu_x)}{|\,\bar{s}-\bar{\mu}\,|^3|\,\bar{\xi}-\bar{\mu}\,|}\ , \tag{20}$$

where the suffixes x and y are the components of the local coordinate. In order to simplify the expansive formulation, the origin rotates or transfers from the global coordinate to each center of multipole as shown in Fig. 1. Therefore, unite outward normal vectors of local coordinate $(n_x(\bar{s}),\ n_y(\bar{s}))$ are equal to (0,1) for an exterior acoustic problem. Substituting unite outward normal vectors into Eqs. (11) ~ (15) and (18), the component of $n_x(\bar{s})$ can be eliminated.

Thus, the kernel functions have been expanded into a series form. Since the kernels become singular as $\bar{s}$ approaches $\bar{\xi}$, the matrix coefficient is calculated in two parts — integration of the regular element and singular element. This integration is discussed as follows.

(1) For a regular element:

In this case, the kernel functions are expanded into series form. The component of matrix can be developed in the following formula [12,21]

$$\begin{aligned} B_{\alpha\beta}(\bar{\xi},\ \bar{s}) &= \int_{\Gamma_\beta} G^R d\Gamma_\beta \\ &= -\frac{i}{4}\sum_{m=0}^{\infty}\varepsilon_m\left[H_{2m}^{(2)}\left(k\,|\,\bar{\xi}-\bar{\mu}\,|\right)\cos(2m\theta)\right. \\ &\quad \left.+H_{2m}^{(2)}\left(k\,|\,\bar{\xi}-\bar{\mu}'\,|\right)\cos(2m\theta')\right] \\ &\quad \times\left[\frac{4}{k}\sum_{n=0}^{\infty}J_{2m+2n+1}(0.5l_\beta k)\right] \\ &\cong \sum_{m=0}^{M}(C_{\alpha,\beta,m}^1+C_{\alpha,\beta',m}^1)R_{m,\beta} \end{aligned} \tag{21}$$

where M is a positive integer and used to approximate the sums of the infinite series. The value of $C_{\alpha,\beta,m}^1+C_{\alpha,\beta',m}^1$ is related to the field points. The value $R_{m,\beta}$ is called multipole moment, and it is related to the length of the source element. When the boundary is divided into uniform meshes, $R_{m,\beta}$ is calculated only once. Thus, they are displayed in the following equations:

$$C_{\alpha,\beta,m}^1 = -\frac{i}{4}\varepsilon_m\,H_{2m}^{(2)}\left(k\,|\,\bar{\xi}-\bar{\mu}\,|\right)\cos(2m\theta)\ , \tag{22}$$

$$C_{\alpha,\beta',m}^1 = -\frac{i}{4}\varepsilon_m\,H_{2m}^{(2)}\left(k\,|\,\bar{\xi}-\bar{\mu}'\,|\right)\cos(2m\theta')\ , \tag{23}$$

$$R_{m,\beta} \cong \frac{4}{k}\sum_{n=0}^{M}J_{2m+2n+1}(0.5l_\beta\,k) \tag{24}$$

where l_β is the length of the βth source element Γ_β and ε_m is denoted by

$$\varepsilon_m = \begin{Bmatrix}1\ , & m=0\\ 2\ , & m\neq 0\end{Bmatrix}\ . \tag{25}$$

In Eq. (22), θ is an angle from $\overrightarrow{\mu\xi}$ to $\overrightarrow{\mu s}$. When the angle is located on the interior of the barrier, such as θ_1 and θ_1' in Fig. 2, the value can be calculated by

$$\theta = \cos^{-1}\left(\frac{(\bar{s}-\bar{\mu})(\bar{\xi}-\bar{\mu})}{|\,(\bar{s}-\bar{\mu})\,||\,(\bar{\xi}-\bar{\mu})\,|}\right)\ , \tag{26}$$

$$\theta' = \cos^{-1}\left(\frac{(\vec{s}'-\vec{\mu}')(\vec{\xi}-\vec{\mu}')}{|(\vec{s}'-\vec{\mu}')||(\vec{\xi}-\vec{\mu}')|}\right). \quad (27)$$

On the contrary, when the angle is located on the exterior of the barrier, such as θ_2 and θ_2' in Fig. 2, the value is amended as the next equations since the angle is greater than π.

$$\theta = 2\pi - \cos^{-1}\left(\frac{(\vec{s}-\vec{\mu})(\vec{\xi}-\vec{\mu})}{|(\vec{s}-\vec{\mu})||(\vec{\xi}-\vec{\mu})|}\right), \quad (28)$$

$$\theta' = 2\pi - \cos^{-1}\left(\frac{(\vec{s}'-\vec{\mu}')(\vec{\xi}-\vec{\mu}')}{|(\vec{s}'-\vec{\mu}')||(\vec{\xi}-\vec{\mu}')|}\right). \quad (29)$$

Taking the normal derivative, with respect to the normal vector, at source points for the kernel function $G(\vec{\xi}, \vec{s})$, the value of $A_{\alpha\beta}$ can also be computed by [12,21]

$$\begin{aligned} A_{\alpha\beta}(\vec{\xi}, \vec{s}) &= \int_{\Gamma_\beta} G_n^R d\Gamma_\beta \\ &= -\frac{ik}{4}\sum_{m=0}^{\infty}\left\{H_{2m+1}^{(2)}\left(k|\vec{\xi}-\vec{\mu}|\right)\sin\left[(2m+1)\theta\right]\right. \\ &\quad \left. - H_{2m+1}^{(2)}\left(k|\vec{\xi}-\vec{\mu}'|\right)\sin\left[(2m+1)\theta'\right]\right\} \\ &\quad \times (R_{m,\beta} + R_{(m+1),\beta}) \\ &\cong \sum_{m=0}^{M}(C_{\alpha,\beta,m}^2 + C_{\alpha,\beta',m}^2)(R_{m,\beta} + R_{(m+1),\beta}), \end{aligned} \quad (30)$$

where the value $C_{\alpha,\beta,m}^2 + C_{\alpha,\beta',m}^2$ is defined in the following equations, respectively:

$$C_{\alpha,\beta,m}^2 = -\frac{ik}{4}H_{2m+1}^{(2)}\left(k|\vec{\xi}-\vec{\mu}|\right)\sin\left[(2m+1)\theta\right], \quad (31)$$

$$C_{\alpha,\beta',m}^2 = -\frac{ik}{4}H_{2m+1}^{(2)}\left(k|\vec{\xi}-\vec{\mu}'|\right)\sin\left[(2m+1)\theta'\right]. \quad (32)$$

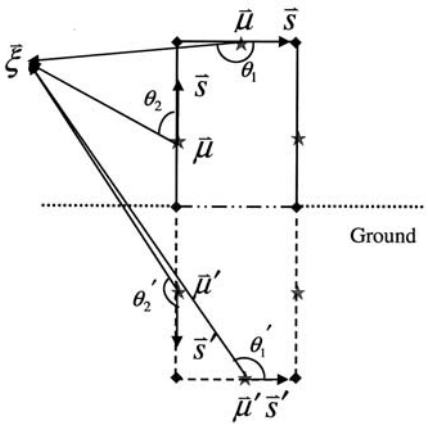

Fig. 2 The angles locat interior/exterior of the barrier

(2) For a singular element:

In this case, the integration of the two kernels can be derived by the conventional BEM. As for the weak singular integral, it led to the limiting form for small arguments in the formula so that the coefficient could be derived from the next equation

$$\begin{aligned} B_{\beta\beta}(\vec{\xi}, \vec{s}) &= \int_{\Gamma_\beta} G d\Gamma_\beta \\ &= -\frac{l_\beta}{4}\frac{2}{\pi}\int_0^1 \ln\left(k\eta\frac{l_\beta}{2}\right)d\eta \\ &\quad + \frac{1}{4i}\sum_{m=0}^{\infty}\varepsilon_m H_{2m}^{(2)}\left(k|\vec{\xi}-\vec{\mu}'|\right)\cos(2m\theta') \\ &\quad \times \left[\frac{4}{k}\sum_{n=0}^{\infty}J_{2m+2n+1}(0.5 l_\beta k)\right] \\ &\cong -\frac{l_\beta}{2\pi}\left[\ln\left(k\frac{l_\beta}{2}\right)-1\right] + \sum_{m=0}^{M}C_{\alpha,\beta',m}^1 R_{m,\beta}. \end{aligned} \quad (33)$$

In Eq. (33), when an independent variable of Hankel function limits to zero that approximates to the next equation [21]

$$iH_0^{(2)}(\zeta) \cong \frac{2}{\pi}\ln(\zeta), \quad (34)$$

where ζ is an argument.

For the strongly singular integral, since the constant element is used in this study, the value of the coefficient can be evaluated as in the next equation

$$\begin{aligned} A_{\beta\beta}(\vec{\xi}, \vec{s}) &= \int_{\Gamma_\beta}\frac{\partial G}{\partial n(\vec{s})}d\Gamma_\beta + \frac{1}{2} \\ &= -\frac{ik}{4}\sum_{m=0}^{\infty}H_{2m+1}^{(2)}\left(k|\vec{\xi}-\vec{\mu}'|\right)\sin\left[(2m+1)\theta'\right](R_{m,\beta}+R_{(m+1),\beta}) + \frac{1}{2} \\ &\cong \sum_{m=0}^{M}C_{\alpha,\beta',m}^2(R_{m,\beta}+R_{(m+1),\beta}) + \frac{1}{2}. \end{aligned} \quad (35)$$

4. NUMERICAL RESULTS

There have been two illustrations selected from Ref. 5 to verify this method. The first one is a rectangular barrier with a height (H_r) of 3m and thickness (T_r) of 0.2m. The insertion loss along a level line at 250Hz is analyzed. The coordinates of the source are (−7.5, 0.5) and the receiver is placed 1.5m from the ground. The numerical result of the present method is shown in Fig. 3. When compared with the analysis of Muradali and BEM, the agreement is good. The next example is the frequency response of the rectangular barrier, where the height and thickness of the rectangular barrier are 3m and 0.2m, respectively. In this case the receiver is located at point (22.5, 3). Figure 4 exhibits the results of insertion loss at different frequencies. It can be seen that the agreement is also good. It shows that the prediction by FMM is reliable.

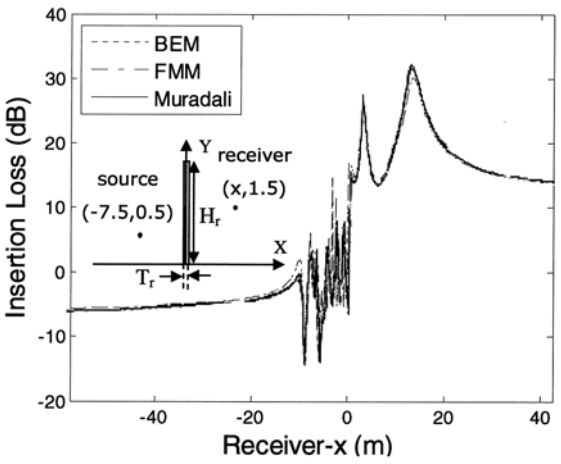

Fig. 3 The insertion loss of rectangular barrier along a line at 250Hz (N = 620)

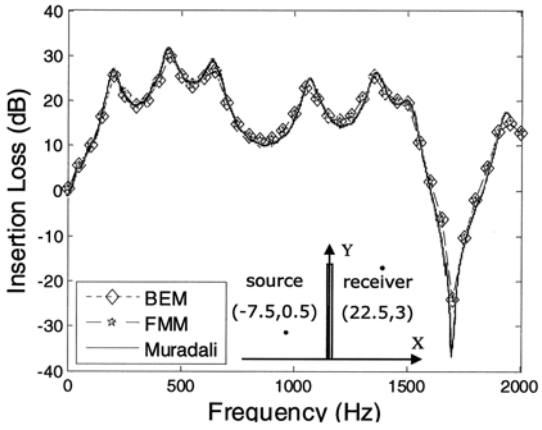

Fig. 4 The frequency response of rectangular barrier (N = 620)

An important parameter concerning the use of FMM is the computing time. To illustrate the benefit of FMM, a comparison of the CPU time between FMM and BEM for different meshes is shown in Fig. 5. The result clearly shows that the FMM reduces the CPU time from the order of N^2/1,180 operations to N/2,500 $\log^{2.5}N$, where N is the number of unknowns. For the reasons mentioned above, FMM is a valid method to accelerate the speed of calculation.

Further, since the kernel is expanded with an infinite series, how many terms needed to achieve the requirement of accuracy is important. If too many terms are required, it will reduce the efficiency of the present method. Figures 6(a) and 6(b) show the insertion loss versus the Mth partial sum in approximating the infinite series in Eqs. (21) and (30). Figure 6(a) shows the sum of the series at a frequency of 50Hz. The numerical results of the boundary mesh of 310, 620, and 1,240 elements are accurate to two decimal places. It was found that the accuracy seems acceptable when two terms are used to approximate the infinite series. Figure 6(b) is similar in its analysis for a frequency of 2,000Hz with 620 and 1,240 elements. Since the constant element is considered in this study and a

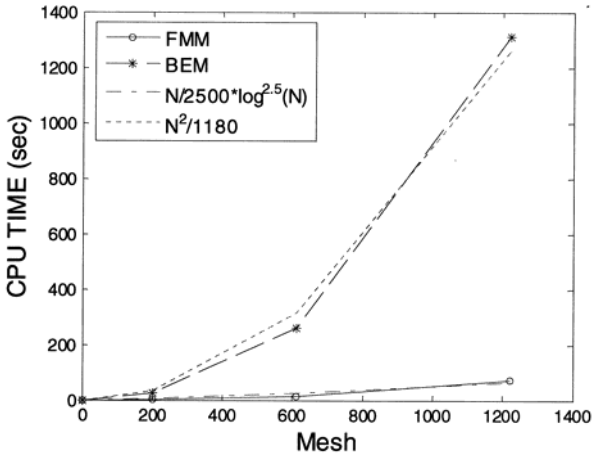

Fig. 5 The result of CPU time versus different mesh for the rectangular barrier

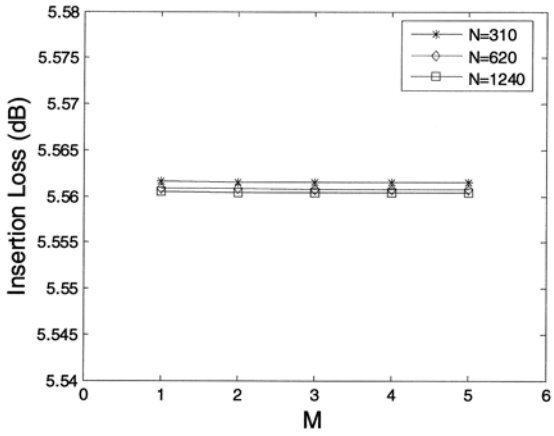

(a) Frequency at 50Hz

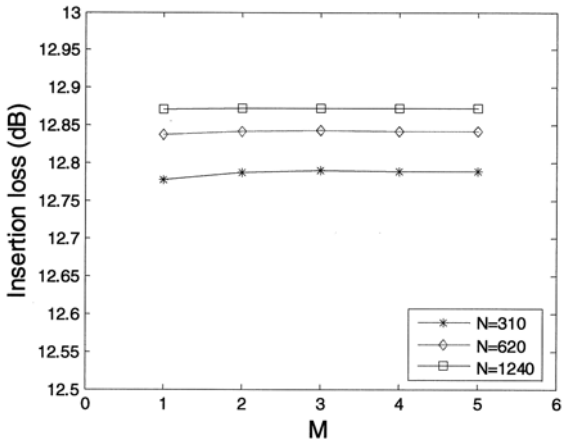

(b) Frequency at 2000Hz

Fig. 6 The insertion loss versus the Mth partial sums of the infinite series

wavelength must include about six to eight nodes, the mesh of 310 elements is not taken into consideration. Similarly, two terms partial sum can also give accurate results. Therefore, the indexes m and n in the degenerated kernel functions are chosen only from 0 to 1, *i.e.* only two terms, in all the following analyses.

Figure 7 shows the insertion loss of rectangular, *T*-shaped, and *Y*-shaped barriers with the same height (H_r, H_t and H_y) and thickness (T_r, T_{t1} and T_{y1}). The dimensions of the *T*-shaped and *Y*-shaped barriers are displayed in Fig. 7; the height and thickness of the rectangular barrier are 3m and 0.2m, respectively. The source and receiver are located the same as in the case of Fig. 3. It is seen that the *Y*-shaped barrier has the best performance when the receiver-x is greater than 20m. The results of the rectangular and T-shaped barriers have the similar insertion loss when the receiver is located at the side of the source. Further, when the receiver is located at a point (22.5, 3), the insertion loss curves for different frequencies are shown in Fig. 8. The results clearly show that the rectangular barrier has fine performance at about 1,350 to 1,500Hz. Further, there is an interesting phenomenon when the insertion losses of rectangular, *T*-shaped, and *Y*-shaped barriers are lowest, about −20dB at 1,700Hz. Above this frequency, the situation is reversed and the *T*-shaped and *Y*-shaped barriers obviously have better insertion loss.

According to the cases in Fig. 8, the following analyses will concentrate on the insertion loss along a line (the vertical coordinate of the receiver fixed at 3m from the ground) for *T*-shaped and *Y*-shaped barriers at a frequency of 1,700Hz. Figure 9 shows the insertion loss of the *T*-shaped barrier with different spans in which the other dimensions are remain the same, as in the previous case, in which H_t = 3m, T_{t1} = 0.2m, T_{t2} = 0.14142m. According to the results, it clearly shows that the vast span (*e.g.*, 1.9m) causes better capability when the receiver is placed on the opposite side of the source. When comparing the insertion loss of a *T*-shaped barrier with different spans on opposite sides, such as L_{t1} = 1.4m, L_{t2} = 0.9m and L_{t1} = 0.9m, L_{t2} = 1.4m, it is found that the barrier with the larger span installed on the sound source side seems to have better performance.

Finally, a *Y*-shaped barrier, with the same height and thickness (H_y = 3m, T_{y1} = 0.2m) and span (L_{y1} = L_{y2} = 1.4m) is analyzed to investigate the influence of the spread angles on barrier performance. The numerical results for three different angles at 1,700Hz are depicted in Fig. 10. It is noticed that the insertion losses are almost the same when the spread angles are 30°, 45° and 60°. The effect is not obvious. This phenomenon shows that the height and span are important parameters, but the shape (spread angle) is not.

5. CONCLUSIONS

A theoretical approach for evaluating the insertion loss of a barrier is developed in this study. The Fast Multipole Method is adopted to accelerate the speed of calculation. The kernel functions are expended into series form and we approximate the sum of the series by two terms. This study extended FMM to a semi-infinite region problem and the numerical results compared well with the researches of Muradali. According

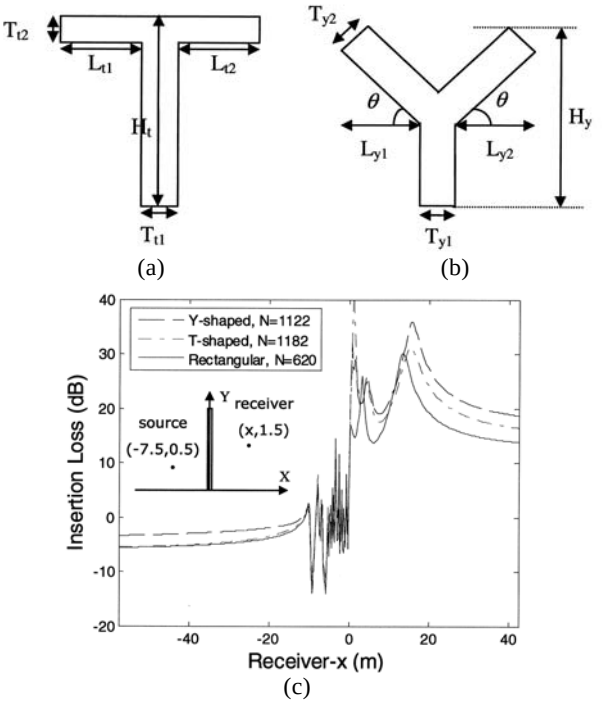

Fig. 7 (a) The geometry of *T*-shaped barrier (H_t = 3m, T_{t1} = 0.2m, T_{t2} = 0.14142m, L_{t1} = L_{t2} = 1.4m). (b) The geometry of *Y*-shaped barrier (H_y = 3m, T_{y1} = 0.2m, T_{y2} = 0.14142m, L_{y1} = L_{y2} = 1.4m, θ = 45°). (c) The insertion loss of rectangular, *Y*-shaped and *T*-shaped barrier at 250Hz

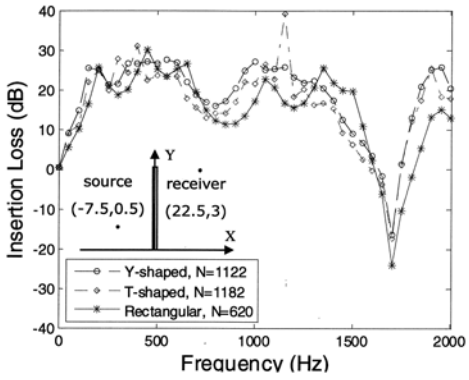

Fig. 8 The frequency response of rectangular, *Y*-shaped and *T*-shaped barrier

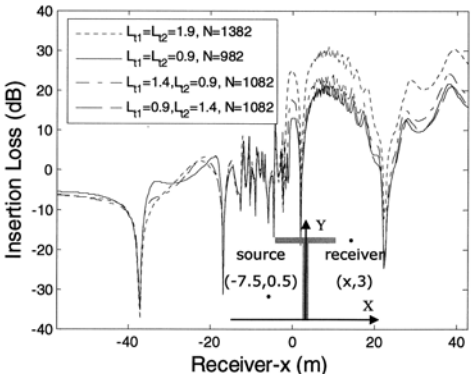

Fig. 9 The insertion loss of *T*-shaped barrier at 1,700Hz (H_t = 3m, T_{t1} = 0.2m, T_{t2} = 0.14142m)

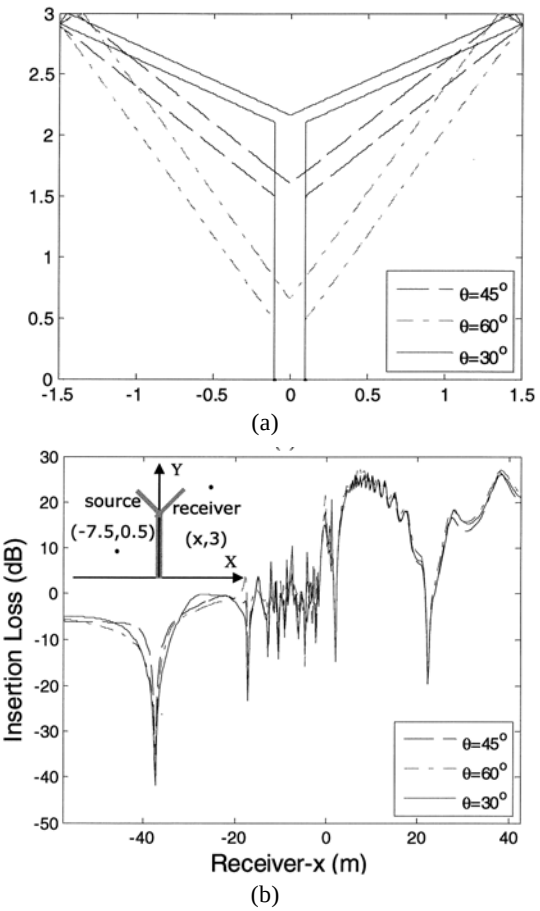

Fig. 10 (a) The dimension of *Y*-shaped barrier with different angles. (b) The insertion loss of *Y*-shaped barrier at 1700Hz (H_y = 3m, T_{y1} = 0.2m, $T_{y2} = T_{y1} * \sin\theta$)

to the cases of this study, the *T*-shaped barrier with wide span cause a better capability and the spread angle of a *Y*-shaped barrier is not an important parameter in the analysis of barriers. In the future this method can be applied to complicated barriers, parallel barriers, or barriers with an absorbing surface.

REFERENCES

1. Hothersall, D. C., Chandler-Wilde, S. N. and Hajmirzae, M. N., "Efficiency of Single Noise Barriers," *Journal of Sound and Vibration*, 146, pp. 303–322 (1991).
2. Kawai, Y. and Terai, T., "The Application of Integral Equations Methods to the Calculation of Sound Attenuation by Barriers," *Applied Acoustics*, 31, pp. 101–117 (1990).
3. Fujiwara, K., Hothersall, D. C. and Kim, C. H., "Noise Barrier with Reactive Surfaces," *Applied Acoustics*, 53, pp. 255–272 (1998).
4. Lam, Y. W., "Using Maekawa's Chart to Calculate Finite Length Barrier Insertion Loss," *Applied Acoustics*, 42, pp. 29–40 (1994).
5. Muradali, A. and Fyfe, K. R., "A Study of 2D and 3D Barrier Insertion Loss using Improved Diffraction-based Methods," *Applied Acoustics*, 53, pp. 49–75 (1998).
6. Chen, J. T. and Chen, P. Y., "A Semi-analytical Approach for Stress Concentration of Cantilever Beams with Holes Under Bending," *Journal of Mechanics*, 23, pp. 211–222 (2007).
7. Lu, C. W., "Numerical Study for Centrifugal Model Tests of a Single Pile Foundation Installed in Sandy Deposits," *Journal of Mechanics*, 23, pp. 389–397 (2007).
8. Wang, C. S. and Wang, Y. C., "The Theoretical and Experimental of Tube Drawing with Floating Plug for Micro Heat-pipes," *Journal of Mechanics*, 24, pp. 111–117 (2008).
9. Hwang, S. F. and Liao, W. T., "Thermal Stress in Discretely Layered Structures with Functional Graded Materials," *Journal of Mechanics*, 24, pp. 297–300 (2008).
10. Rokhlin, V., "Rapid Solution of Integral Equations of Classical Potential Theory," *Journal of Computational Physics*, 60, pp. 187–207 (1985).
11. Greengard, L. and Rokhlin, V., "A Fast Algorithm for Particle Simulations," *Journal of Computational Physics*, 73, pp. 325–348 (1987).
12. Chen, J. T. and Chen, K. H., "Applications of the Dual Integral Formulation in Conjunction with Fast Multipole Method in Large-scale Problems for 2D Exterior Acoustics," *Engineering Analysis with Boundary Elements*, 28, pp. 685–709 (2004).
13. Chen, K. H., Chen, J. T., Kao, J. H. and Lee, Y. T., "Applications of Dual Integral Formulation in Conjunction with Fast Mutipole Method to Oblique Incident Wave Problem," *International Journal for Numerical Methods in Fluids*, 59, pp. 711–751 (2009).
14. Fujiwara, H., "The fast multipole method for solving integral equations of three-dimensional topography and basin problems," *Geophysical Journal International*, 140, pp. 198–210 (2000).
15. Fujiwara, H., "The Fast Multipole Method for Integral Equations of Seismic Scattering Problems," *Geophysical Journal International*, 133, pp. 773–782 (1998).
16. Nishimura, N., "Fast Multipole Accelerated Boundary Integral Equation Methods," *American Society of Mechanical Engineers*, 55, pp. 299–324 (2002).
17. Lacerda, L. A., Wrobel, L. C. and Mansur, W. J., "A Dual Boundary Element Formulation for Sound Propagation Around Barriers over an Impedance Plane," *Journal of Sound and Vibration*, 202, pp. 235–247 (1997).
18. Chen, J. T., Chen, I. L. and Chen, K. H., "Treatment of Rank-Deficiency in Acoustics Using SVD," *Journal of Computational Acoustics*, 14, pp. 157–183 (2006).
19. Seybert, A. F. and Rengarajan, T. K., "The Use of CHIEF to Obtain Unique Solutions for Acoustic Radiation Using Boundary Integral Equations," *Journal of the Acoustical Society of America*, 81, pp. 1299–1306 (1987).
20. Burton, A. J. and Miller, G. F., "The Application of Integral Equation Methods to the Numerical Solution of Some Exterior Boundary Value Problems," *Proceeding of the Royal Society of London. Series A, Mathematical and Physical Sciences*, 323, pp. 201–210 (1971).
21. Abramowitz, M. and Stegun, I. A., *Handbook of Mathematical Functions with Formulas, Graphs and Mathematical Tables*, New York, Dover (1965).

(Manuscript received December 11, 2007, accepted for publication February 17, 2008.)